The Role of Open Cell Foams Supports on the Kinetics of PdO/Co3 O4 for the Wet and Dry Lean Methane Combustion

ChemCatChem

ChemCatChem
Chemistry Europe
European Chemical Societies Publishing

RESEARCH ARTICLE OPEN ACCESS

The Role of Open Cell Foams Supports on the Kinetics of PdO/Co_3O_4 for the Wet and Dry Lean Methane Combustion

Hernan G. Mazzei[1] | Roshni S. Kumar[2] | Natalia Semagina[2] | Paweł Stelmachowski[3] | Andrzej Kotarba[3] | Stefania Specchia[1]

[1]Department of Applied Science and Technology, Politecnico Di Torino, Torino, Italy | [2]Department of Chemical and Materials Engineering, University of Alberta, Edmonton, Canada | [3]Faculty of Chemistry, Jagiellonian University, Kraków, Poland

Correspondence: Hernan G. Mazzei (hernan.mazzei@polito.it) | Stefania Specchia (stefania.specchia@polito.it)

Received: 23 December 2025 | **Revised:** 22 February 2026 | **Accepted:** 23 February 2026

Keywords: alumina | FeCrAlloy | heterogeneous catalysis | silicon carbide | supported catalysts | water deactivation

ABSTRACT

In this study, a kinetic analysis under differential conditions was conducted on three different open cell foams (OCFs) materials—FCA(FeCrAl)-OCF, SiC(silicon carbide)-OCF, and Alu(alumina)-OCF—washcoated with a PdO/Co_3O_4 catalyst for lean methane combustion in both dry and wet environments (10 vol% H_2O). A comprehensive set of physicochemical characterizations, including CO chemisorption, FESEM, XRD, Raman spectroscopy, XPS, XRF, TPR, TPO, and TPD, was performed on the supported catalysts. All structures demonstrated comparable catalytic activity and excellent water stability over time. The activation energy was consistent across all catalytic systems, with values of approximately 117 kJ mol^{-1} in dry conditions and 129 kJ mol^{-1} in wet conditions. While all catalysts exhibited first-order kinetics with respect to methane, variations in water order were observed: –0.9 for Alu-OCF, –0.7 for FCA-OCF and SiC-OCF. Additionally, the preexponential factors in wet conditions followed the order Alu-OCF > SiC-OCF > FCA-OCF, which corresponded with the order of turnover frequencies. Validation of the kinetic modeling results was performed against the experimental data. The hydrophobicity of the supports appeared to play a role in water inhibition, with SiC-OCF, the most hydrophobic of the materials tested, demonstrating superior catalytic activity.

1 | Introduction

Methane is receiving increased attention due to its consistent rise of over 150% since 1750, coupled with its potent warming impact [1]. Methane significantly contributes to the greenhouse effect, responsible for approximately a quarter of global warming. Over a 20 year period, methane has a GWP (Global Warming Potential) of 86 times that of CO_2, and over a century, it is 28 times higher [2]. Its abatement also drives the development of efficient technologies to break the strong C–H bonds, since it is a very stable molecule. One of the main sources of methane emissions is the transportation sector. In particular, natural gas, which is mainly composed of methane, offers several advantages compared to other conventional fuels, including cleaner emissions, efficient fuel use, and abundance [3]. Natural gas engines can also operate in lean conditions, minimizing the typical products of incomplete combustion compared to stoichiometric conditions. However, unburnt methane released into the atmosphere in the exhaust gases presents a significant challenge. Thus, efficient catalytic converters must be developed to avoid these fugitive emissions [4]. Pd-based catalysts are considered the most active catalysts for the total oxidation of methane. However, limited availability and high cost of Pd led to an investigation into transition metal oxides for its total or partial replacement [5, 6].

Additionally, real exhaust gas systems also contain sulfur and water vapor in the stream, which can contribute to the deactivation of the catalyst. While sulfur poisoning is typically not a

concern in the exhaust of natural gas engines due to the low sulfur content of natural gas, water is a significant catalytic poison for methane combustion, especially because of its high content (>10 vol%) [7, 8]. Water, originating from the combustion process or forming during catalytic methane conversion, can cause chemical and morphological changes in Pd catalysts during CH_4 oxidation. The deactivation process reduces the lifetime of palladium-based catalysts, necessitating frequent maintenance and substitution operations, thereby increasing overall system costs. The inhibitory effect of water on Pd-based catalysts depends on various factors, including water concentration, catalyst formulation, time on stream history, and reaction temperature. Water adsorption on Pd sites can disrupt the transfer of oxygen from the support to Pd sites, limiting the availability of O-Pd site pairs and impeding catalyst activity [9].

To address these challenges, supported Pd-based catalysts are considered promising alternatives [10]. The metal-support interaction plays a crucial role in affecting the stability and dispersion of Pd catalysts, as well as the rate of sintering. The properties of oxide supports, such as acid strength and oxygen surface mobility, influence Pd-support interactions, affecting Pd oxidation state, dispersion, and hydroxyl accumulation. Supports with higher oxygen surface mobility can decrease the inhibitory effect of H_2O on PdO catalysts by enhancing the desorption rate of hydroxyl groups during CH_4 oxidation, resulting in increased resistance to water inhibition [11, 12]. In particular, Pd-based catalysts supported on cobalt spinel oxide have been reported to exhibit a synergistic effect, enhancing both the activity and stability of the catalyst. Cobalt oxide exhibits optimal oxygen binding energy and redox properties that facilitate strong metal support interactions and influence the Pd/PdO transformation process, particularly under wet conditions [13, 14]. While cobalt oxide does not prevent the formation of inactive $Pd(OH)_2$, its ability to activate and supply oxygen species makes it a valuable support for Pd-catalyzed methane combustion in wet environments [15, 16]. Cobalt oxide itself also exhibits catalytic activity in methane combustion and may contribute up to 70% of the catalytic activity to Pd, especially at lower temperatures and higher water concentration [17].

During the last couple of years, monoliths have emerged as the predominant and well-established catalytic support, particularly in the treatment of automobile exhaust gases. Monolithic structures offer significant advantages, including a short diffusion path in the catalyst layer, a high external surface area, rapid interfacial mass transfer rates, and low-pressure drop in the monolith channels. These advantages contribute to lower investment costs and increased productivity in manufacturing operations. However, monolith supports also come with some drawbacks, such as poor radial heat transfer coefficients due to the absence of radial mixing, potential nonuniform fluid distribution, and limitations in temperature control due to their essentially adiabatic nature [18–20]. Open-cell foams (OCFs) have emerged as highly promising alternatives for catalytic support in process intensification, leveraging their distinctive properties. The intricate geometry of OCFs enhances local mixing and gas-to-solid transport by interacting strongly with the flow field, leading to continuous boundary layer formation and disruption, ultimately improving transport properties. OCFs offer numerous benefits, including a high specific surface area, low-pressure drops, excellent chemical resistance, high thermal stability, and mechanical strength. Additionally, they enhance heat and mass transfer due to tortuous flow paths through the porous matrix [21, 22]. These materials are also attractive for thermal management applications, such as heat exchangers, heat sinks, and heat pipe wicks [23–25]. Thermally conductive foams and monoliths enhance radial heat transfer, enabling operation under more extreme process conditions while mitigating the risk of catalyst deactivation due to overheating and preventing reactor runaway. In contrast to conventional honeycomb monoliths, OCFs allow for radial dispersion of the flow, promoting the uniform distribution of reactants across the catalyst bed. This high effectiveness is beneficial for reactors designed for high transfer coefficient conditions and high catalyst effectiveness. OCFs can be described as irregular cellular materials composed of interconnected solid struts, forming a continuous three-dimensional network enclosing empty regions called cells [26, 27]. Due to these favorable structural properties, OCFs have the potential to serve as enhanced catalyst carriers, replacing randomly packed beds of pellets in tubular reactors. OCFs have found applications in a range of reactions, including volatile organic compounds oxidation, methanol and Fischer-Tropsch synthesis, catalytic wet peroxide oxidation, preferential oxidation of CO, partial oxidation of methanol, complete combustion of methane, removal of soot from diesel exhaust, and endothermic processes like steam reforming [28–32]. Ceramic structures are characterized by better adhesion between the catalyst and the foam, high thermal resistance, and strength, while metal structures exhibit greater thermal conductivity and resistance to mechanical shock. However, ceramics may crack with significant temperature changes, and metals may corrode or fuse at high temperatures due to limited thermal stability [33, 34].

The flow and dispersion of catalysts within the foam cells can affect the reaction kinetics. However, the study of the mechanism has long been a challenging aspect in this field, resulting in the limited scale-up of the catalytic process based on foam substrates. While the geometrical characteristics and thermal conductivity of OCFs have been investigated to influence the performance of reaction and transport phenomena, studies have shown that the choice of support material can significantly impact the catalytic reaction itself. The interaction between the support and the active catalyst material can affect factors such as catalytic activity, selectivity, and stability, demonstrating that the catalyst's support is not merely a passive component but plays an active role in the overall reaction dynamics [35–38].

The influence of support materials on catalytic performance has been extensively studied, highlighting the significant roles of both the physical structure and chemical interactions between the support and the active phases. For instance, research has shown that Co_3O_4-Cs deposited on Al_2O_3 ceramic foam exhibited the highest specific rate constant for N_2O decomposition among various supported samples. This superior performance was attributed to the enhanced dispersion of the active phase and its interaction with the Al_2O_3 support [39]. Similarly, studies have demonstrated that cation diffusion from the catalytic layer to the metallic monoliths, and vice versa, can alter the catalytic formulation, thereby affecting CO oxidation properties. The extent and nature of these modifications are dependent on the catalyst composition, the metallic substrate, and the reaction conditions [40]. Further investigations have revealed that metal foams can directly

influence the activity of the catalyst layer through the diffusive penetration of metal atoms from the foam into the catalyst [41]. Specifically, the use of nickel foams has been shown to enhance the crystallization of the active PdO phase during methane combustion [42]. A comparative study of ceramic and metallic monoliths for VOC abatement attributed differences in catalytic activity primarily to variations in thermal conductivity, while also acknowledging the potential for catalyst modification during deposition or due to interactions with the structured substrate [43]. Lastly, it has been observed that the synthesis of mordenite is influenced not only by the morphological characteristics of the support but also by chemical diffusion processes, which can alter the theoretical formulation of the catalyst [44].

Concerning combustion in the presence of water vapor, several studies have highlighted the superior stability and water tolerance of SiC-supported catalysts in high-temperature and hydrothermal environments. For instance, experiments conducted on Pd catalysts supported by SSZ-39 zeolites demonstrated that a high Si content significantly enhances structural stability, with hydrothermal aging at 1000°C causing no noticeable degradation. These catalysts showed minimal deactivation after 105 h on stream at 750°C in the presence of 2.7 vol% water [45]. Additionally, the development of Co/β-SiC catalysts has proven their superior water tolerance and stability under high water partial pressures when compared to traditional Co/Al_2O_3 catalysts, owing to the chemical inertness and hydrothermal stability of SiC [46]. The use of SiC as a support material also increases the specific surface area, promoting better molecular diffusion and transport, which further enhances resistance to water toxicity and improves catalytic performance in humid environments [47]. A Co@S1/SiC-40 h catalyst displayed exceptional stability, with negligible deactivation observed during a 200 h longevity test, underscoring its excellent moisture tolerance and prolonged activity in water-containing reaction conditions [48].

Although specific studies comparing catalytic deactivation using FeCrAl as a support are limited, there is evidence highlighting its potential advantages in high-stress environments [49, 50]. Kim et al. [51] stated that FeCrAl's metal structure minimizes hot spots and the superficial α-Al_2O_3 layer not only protects the material but also stabilizes active sites, reducing the rate of thermal deactivation. However, challenges remain. For instance, one study reported rapid deactivation of an $Ir/Ce_{0.8}Zr_{0.2}O_2$/FeCrAl catalyst during the water-gas shift reaction due to poor coating adhesion and subsequent loss of active components [52]. Additionally, material degradation at high gas hourly space velocity has been observed, leading to shifts in product composition and temperature, with SiC monoliths proving more stable under similar conditions [53]. Despite these issues, FeCrAl alloys demonstrate excellent resistance to hydrothermal corrosion, particularly in light water reactor environments, largely due to their chromium content [54].

In this study, the reaction kinetics of methane combustion under lean conditions were systematically investigated using different foam substrates washcoated with a PdO/Co_3O_4 catalyst. The influence of the structural support was examined by comparing the catalytic performance of foams composed of alumina, silicon carbide, and FeCrAl alloy (denoted as Alu-OCF, SiC-OCF, and FCA-OCF, respectively). The analysis was conducted under both dry conditions and in the presence of 10 vol% water in the feed to simulate wet conditions. Methane concentration was maintained at 1 vol%, with a fixed CH_4/O_2 molar ratio of 8, and a WHSV (weight hourly space velocity) of 30 NL h^{-1} $g_{cat}{}^{-1}$. Kinetic studies were performed under differential conditions following the hydrothermal aging (HTA) of the catalytic systems, ensuring stable performance despite partial deactivation. The structured catalysts were characterized using CO chemisorption, X-ray diffraction (XRD), Raman spectroscopy, field-emission scanning electron microscopy (FESEM), and scanning electron microscopy (SEM), X-ray fluorescence (XRF), X-ray photoelectron spectroscopy (XPS), temperature programmed reduction in H_2 (H_2-TPR), temperature programmed oxidation and desorption in O_2 (O_2-TPO and O_2-TPD) techniques. The primary objective of this work was to elucidate the kinetic effects associated with different support materials and to assess whether these materials could enhance catalytic activity and stability during lean-burn methane combustion in wet environments.

2 | Materials and Methods

2.1 | Open Cell Foams and Chemicals

Silicon carbide (SiC-OCF) and alumina (Alu-OCF) ceramic open-cell foams with a pore density of 45 ppi (Vukopor HT) were purchased from Lanik s.r.o. (Czech Republic). The metallic open-cell foam, made of FeCrAl alloy (FCA-OCF) with a pore density of 40 ppi, was sourced from Metpore (U.S.A.). Each foam sample measured 9 mm in diameter and 30 mm in length. According to the information provided by the manufacturers, SiC-OCF is constituted by 65% SiC, 20% SiO_2, and15% Al_2O_3; Alu-OCF is constituted by 85% Al_2O_3, 14% SiC, and 1% MgO; FCA-OCF is constituted by 70% Fe, 21% Cr, 9% Al, and traces of Zr, Y, and Mn. The chemicals used in this study were sourced from Sigma-Aldrich, including cobalt(II) nitrate hexahydrate ($Co(NO_3)_2{\cdot}6H_2O$, ≥98% purity), palladium(II) nitrate hydrate ($Pd(NO_3)_2{\cdot}xH_2O$, ≥99% purity), glycine (NH_2CH_2COOH, ≥99% purity), isopropyl alcohol ($CH_3CHOHCH_3$, ≥99.7% purity), and ethanol (CH_3CH_2OH, ≥99.8% purity). The suspension preparation involved polyvinyl alcohol (PVA) (Mowiol 4-88) and an inorganic colloid (Al_2O_3, Nyacol AL20). Ultrapure water with a resistivity of approximately 18 MΩ·cm was generated using a Millipore Milli-Q system for all aqueous solutions. Methane (9.93 vol% CH_4/N_2, Praxair, certified purity), dry air, and nitrogen gases (Praxair, certified purity) were supplied in cylinders.

2.2 | Preparation of the Coated OCFs

First of all, a 3 wt.% PdO/Co_3O_4 catalyst was synthesized as a powder through a two-step process involving solution combustion synthesis (SCS) followed by wetness impregnation (WI), according to our standardized procedure [55, 56]. Briefly, the cobalt spinel precursor was first prepared by mixing cobalt nitrate with glycine at a 25% of the stoichiometric ratio. This solution was stirred at 120°C and then transferred to an electric oven at 250°C for 15 min to initiate the combustion reaction. The resulting spinel was calcined in static air at 600°C for 4 h. To incorporate palladium, an aqueous solution of palladium nitrate was added drop by drop to the cobalt spinel at approximately 140°C. The

palladium-doped catalyst, with a metal loading of 3 wt.%, was then calcined under the same conditions as the undoped spinel.

Afterwards, structured catalysts were prepared. All foam structures were cleaned in a 50/50 (vol.%) water/acetone solution using an ultrasonic bath at room temperature for at least 30 min, followed by drying at 140°C for 30-60 min. After cleaning, the previously prepared catalyst was applied to the OCFs through a washcoating technique [57, 58]. The coating suspension was prepared by first grinding the calcined catalyst powder in a ball mill at 169 rpm for 5 h. Separately, 2.08 g of PVA was dissolved in 60 g of distilled water at 80°C with constant stirring and then allowed to cool to room temperature. The milled catalyst powder and 2.27 g of NYACOL were sequentially added to the cooled PVA solution, with continuous stirring. The pH of the suspension was adjusted to 3 using nitric acid, and the mixture was stirred continuously for 3 days. OCFs were individually immersed in the suspension at a controlled speed of 3 cm min^{-1}, held in the solution for 1 min, and then withdrawn at the same speed. Excess liquid was removed via centrifugation at 400 rpm for 4 min, followed by drying at 80°C for 30 min. This coating process was repeated until 200 mg of catalyst was deposited on each foam. Finally, the coated foams were calcined at 500°C for 2 h with a temperature ramp of 2°C min^{-1}.

2.3 | Catalytic Testing Toward Lean Methane Combustion

The catalytic performance of each 3 wt% PdO/Co_3O_4 catalyst supported on various open-cell foams (OCFs) was assessed for methane combustion under lean conditions, with a constant O_2/CH_4 molar ratio of 8 maintained throughout the experiments. The catalytic tests were conducted in a tubular reactor comprising an inner tube made of 316 stainless steel ($^3/_8$-inch diameter) and an outer sleeve ($^7/_8$-inch diameter) designed to support the reactor and ensure isothermal conditions (Figure S1 in the Supporting Information). The reactor was situated within an electric tube furnace equipped with a PID temperature controller. ensuring precise thermal regulation. Feed gas flows, including CH_4, dry air, N_2, and H_2O, were controlled using electronic mass flow controllers (Brooks 5850 TR) and a syringe pump (Harvard Apparatus Pump 11 Elite). The gases were mixed before being introduced into the reactor. K-type thermocouples were strategically positioned: two thermocouples within the inner tube (upstream and downstream of the catalyst bed, respectively), and a third one within the outer sleeve. The output gases passed through a cold trap to condense and remove water vapor, and the gas composition was analyzed using an online Agilent HP-7890A gas chromatograph (GC) equipped with both thermal conductivity (TCD) and flame ionization (FID) detectors. The reaction and analysis procedure were described elsewhere [59].

For the wet runs, 10% vol. water was introduced into the reactor using a peristaltic pump (Harvard Apparatus Pump 11 Elite). The water was vaporized before entering the reactor by heating the upstream tubing. HTA of the catalysts was conducted over 45 h to evaluate their stability, with the temperature varying between 450 and 600°C. Ignition-extinction (I-E) tests were performed both before and after HTA under wet conditions, across a temperature range of 200 to 600°C. Data acquisition and experimental monitoring were managed using LabVIEW software. The experiments were conducted with an inlet CH_4 concentration of 1 vol% and an O_2 concentration of 8 vol% in N_2.

For kinetic studies, a differential packed-bed reactor was employed, ensuring conversions below 15%. Each OCF was halved to a length of 1.5 cm. Ignition curves were measured at varying initial methane concentrations (0.3%, 0.5%, 0.8%, and 1%) while maintaining a constant WHSV of 30 NmL h^{-1} $g_{cat}{}^{-1}$. Additional measurements were taken at altered flow rates at WHSV 60 and 15 NmL h^{-1} $g_{cat}{}^{-1}$ for comparison, in both dry and wet conditions. Furthermore, ignition tests were conducted at different water concentrations (3%, 5%, 8%, and 10%) while maintaining constant methane concentration and flow rate constant (1 vol% CH_4 and 30 WHSV).

All measurements were repeated at least 3 times to keep the standard deviation below 3%.

2.4 | Characterization of the Structured Catalysts

CO chemisorption for measuring Pd dispersion in the structured catalyst was carried out using a Micromeritics AutoChem 2950 HP instrument after an in situ reduction pretreatment to ensure that Pd was present predominantly in its metallic state. Each OCF was packed into a stainless steel U-tube with quartz wool. The Pd-supported catalysts were subjected to a reduction in a flow of 5% H_2/He (20 NmL min^{-1}) at 150°C for 1 h, with a ramping rate of 10°C min^{-1}. The sample was then purged with helium (20 NmL min^{-1}) for 30 min at 150°C and cooled to ambient temperature under helium. A dynamic CO pulse chemisorption analysis was performed by dosing a 3% CO/He gas mixture at room temperature. The flow rates for the 3% CO/He loop gas and helium carrier gas were set at 25 and 50 NmL min^{-1}, respectively. Following the CO chemisorption measurements, the Pd-based catalysts were re-oxidized in situ in a 10% O_2/He flow (20 NmL min^{-1}) at 550°C for 1 h, with a ramping rate of 10°C min^{-1}. This was followed by naturally cooling the catalysts down to room temperature under a 10% O_2/He flow. The amount of adsorbed CO was taken as a direct measure of the number of exposed Pd surface atoms. Metal dispersion was calculated assuming a CO-to-surface Pd stoichiometric ratio of 1. The dispersion values derived from CO chemisorption were subsequently used to calculate and plot the apparent turnover frequency (TOF) under the corresponding reaction conditions, using the expressions reported in the Supporting Information. The measurements were performed on fresh samples, and used after the tests.

OCF structures were subjected to XRD analysis using CuK radiation, utilizing an X'pert Pro Philips diffractometer. Data were recorded in the 2θ range of 5–90° with a step size of 0.02°. The crystallite size was calculated using the Scherrer equation.

The Raman spectra of OCFs were recorded at room temperature employing a Renishaw InVia spectrometer, equipped with a Leica DMLM confocal microscope and a CCD detector. The excitation wavelength used was 785 nm. The collected Raman scattered light spanned the spectral range of 100–1400 cm^{-1}. To ensure an ample signal-to-noise ratio, a minimum of five scans were accumulated.

The investigation of the morphology of the catalytic layer on all OCFs was conducted via FESEM (FESEM JEOL-JSM-6700F instrument) and SEM (TM3030Plus TESCAN VEGA3) microscopes.

The elemental composition of cobalt, nickel, palladium, and the OCF substrates was confirmed using XRF analysis, conducted on a Thermo Scientific ARL QUANT'X spectrometer. X-rays were generated with a rhodium (Rh) anode, spanning an energy range of 4–50 kV in 1 kV increments. The XRF detection was carried out using a 3.5 mm silicon (Si) drifted crystal detector, which was Peltier-cooled to approximately 185 K. Quantitative elemental analyses were performed using UniQuant software.

XPS analysis was performed using a Prevac photoelectron spectrometer equipped with a VG SCIENTA R3000 hemispherical analyzer. The measurements utilized a monochromatized AlKα radiation source (E = 1486.6 eV) and an electron flood gun (FS40A-PS) to neutralize any residual surface charge. The background pressure in the analysis chamber was consistently maintained at 5×10^{-9} mbar during data acquisition. Prior to recording the spectra, the samples were outgassed at around 50°C for at least 15 min. Spectra were collected with a pass energy of 100 eV for both survey and narrow scans. Binding energies were calibrated using the C 1s peak at 285 eV, corresponding to adventitious carbon. The surface composition of the samples was analyzed by examining the Co 2p, Pd 3d, O 1s, Al 2p, and Si 2p photoelectron peaks.

Coated OCFs were analyzed via H_2-TPR with a Micromeritics AutoChem 2950 HP instrument, equipped with a thermal conductivity detector (TCD). Before TPR experiments, the samples were subjected to an oxidation treatment in a 10% O_2/He gas mixture (20 NmL min^{-1}), where the temperature was ramped from 120°C to 400°C and maintained at 400°C for 1 h. Following this oxidation step, the samples were cooled to 120°C under a helium atmosphere. The H_2-TPR analysis was then conducted by heating the samples in a 5% H_2/He gas mixture (20 NmL min^{-1}) up to 700°C. After the H_2-TPR process, the samples were flushed with He (20 NmL min^{-1}) for 30 min at 700°C and subsequently cooled down to 120°C. To determine the reduction energy (E_{red}), H_2-TPR experiments were performed at six different heating rates (β = 2.5, 5, 7.5, 10, 12.5, and 15°C min^{-1}) for each oxide support. Between each heating rate, the oxide supports were purged with He and reoxidized in a 10% O_2/He atmosphere (20 NmL min^{-1}) with the temperature increased from 120°C to 400°C and held at 400°C for 1 h. H_2-TPR analysis provided only qualitative results of the samples.

The same equipment was used to evaluate the oxidation temperature with the O_2-TPO analysis. The samples were exposed to 10% O_2/He (20 NmL min^{-1}) from 120°C to 400°C at a rate of 10°C min^{-1} and held at 400°C for 1 h. Afterwards, the oxidized samples were cooled to 120°C in He. The amount of O_2 consumed during the experiment was used to estimate PdO content after oxidation.

The samples were analyzed by O_2-TPD in a quartz flow reactor with sintered glass. Before treatment, each sample was heated in an oxygen flow to 600°C and cooled with helium to 120°C. O_2-TPD involved feeding helium from 120°C to 700°C at a heating rate of 10°C min^{-1}. The signal was recorded using a Hiden Analytical QMS detector.

2.5 | Reactor Modelling and Optimization

The experimental data were processed using MATLAB to determine the reaction order and calculate activation energies based on the power law model. The kinetic analysis was performed at differential conditions. The design equations for the packed—bed reactor applied to the system are explained and reported in the Supporting Information. The same for the Arrhenius expression used to determine the activation energy and pre-exponential factor.

To ensure the measurement of intrinsic kinetics, it was essential to operate within a reaction regime devoid of mass transfer limitations. This was verified using the Carberry number (Ca) to assess external mass transfer, and the Weisz-Prater criterion (WP) for internal mass transfer limitations [60, 61]. Instead, Mears (X) and Anderson (ψ) criteria were used to evaluate external and internal heat transfer limitations respectively [62, 63] (see Supporting Information).

3 | Results and Discussion

3.1 | Physicochemical Analysis

Table 1 presents the CO chemisorption data for the thermally treated PdO/Co_3O_4-coated OCFs, before starting the catalytic tests. Considering the in situ reduction pretreatment to ensure that Pd was present predominantly in its metallic state, we considered CO uptake dominated by adsorption on metallic Pd sites. While contributions from oxidic species such as Co_3O_4 cannot be completely excluded, these interactions are expected to be weak and reversible and therefore negligible for the purpose of dispersion calculations [64]. Furthermore, all OCF substrates appear entirely covered by the Pd/Co_3O_4 coating, even if some cracks are visible from FESEM images (Figure 2). Therefore, the coating should minimize any direct interaction between the foam support and CO. This fact, together with the very low specific surface area of the supports themselves allows considering negligible any contribution from the support. Measurements carried out on Pd/Co_3O_4 powder catalyst exhibited a Pd crystallite size of 3.3 nm with a metal dispersion of 33.2%. However, when this catalyst was deposited onto the OCF structures, the crystallite size significantly increased, resulting in a marked decrease in metal dispersion compared to the pure powder form. This increase in crystallite size is attributed to sintering processes during prior calcination. Additionally, the washcoating process may have been uneven, leading to a dilution effect and irregular catalyst distribution across the supports. Notably, the metallic OCFs displayed the smallest crystallite size and highest metal dispersion among all the structures tested.

Figure 1A displays the XRD patterns for all coated OCFs. Although the patterns include peaks from the OCF material's structural components, which make the analysis more complex, distinct peaks corresponding to cobalt oxide and, in most cases, PdO are observed. Table 1 also presents the Co_3O_4 crystallite

TABLE 1 | Chemisorption and XRD characterizations over OCFs coated catalysts.

Catalyst –OCF(PdO/Co_3O_4)	PdO dispersion[a] (%)	PdO surface area[a] ($m^2\ g^{-1}$ metal)	PdO crystal size[a] (nm)	Co_3O_4 crystal size[b] (nm)
Alu–OCF	2.1	9	46	45
SiC–OCF	4.6	20	21	24
FCA–OCF	7.9	34	12	23

[a]From CO chemisorption.
[b]From XRD.

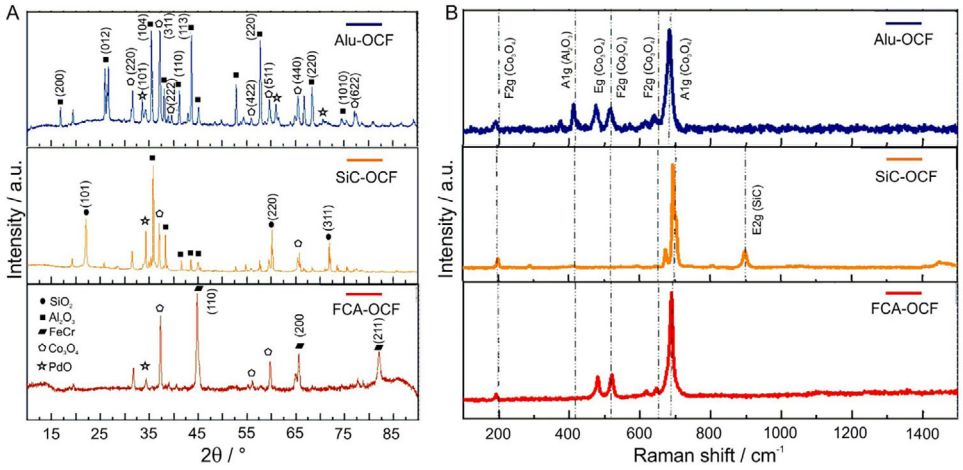

FIGURE 1 | XRD patterns (A) and Raman spectra (B) of PdO/Co_3O_4 coated OCFs.

sizes derived from these structures, showing similar values for the SiC-OCF and FCA-OCF, while the Alu-OCF exhibits a larger crystallite size for the spinel cobalt oxide. Raman spectroscopy is more sensitive for detecting phase impurities compared to x-ray diffraction. It was thus employed to study the phase composition of the investigated materials. The analysis identified five active Raman modes characteristic of the spinel structure at 196, 482, 522, 619, and 691 cm^{-1}, confirming the presence of nanocrystalline Co_3O_4. These modes correspond to the Eg, 3x F2g, and A1g vibrational modes of crystalline Co_3O_4, respectively (Figure 1B). The high-frequency A1g peak is primarily associated with vibrations of octahedral cations in the normal spinel, while the F2g and Eg modes involve both tetrahedral and octahedral site vibrations. A slight shift observed in the SiC support suggests potential interactions between the phases. Furthermore, the presence of carbon might influence the catalyst structure, as indicated by the absence of the Eg and A2g modes of cobalt oxide. Due to the low concentration of PdO, its characteristic vibrational band at 640 cm^{-1} was not detected.

Figure 2 shows the morphological characteristics of the OCFs, displaying FESEM and SEM images of both bare and coated structures. These images reveal a uniformly coated surface, with a thin catalyst layer evenly covering the entire geometric area of the OCF. Notably, the characteristic shape of Co_3O_4 spinel crystals is visible, forming clusters of truncated octahedra. The catalytic layer appears uniformly distributed and securely adhered across all structures, with no evidence of superficial debris, even if some cracks in the coating are visible here and there.

The XRF analysis of the Co_3O_4 phase reveals variations in phase composition and loading across the samples, as detailed in Table 2. This elemental analysis provides both qualitative and quantitative insights into the sample compositions. In ceramic-coated OCFs, a consistent and uniform distribution of cobalt spinel oxide is observed, though slight variations in PdO levels suggest potential imperfections in the washcoating process and the inherent uncertainties of the standardless XRF method. In contrast, metallic-coated OCFs exhibit lower relative quantities, which could be linked to the lower stability of the washcoat over metallic OCFs, as they experience thermal expansion, making it more difficult for the washcoat to adhere to the support.

The surface chemical composition and oxidation states of the catalysts were investigated by XPS, and Table 3 summarizes the results. A consistent oxygen content was observed across all samples. Noteworthy, the metallic-OCF sample exhibited a high concentration of cobalt but a significantly lower palladium content compared to the rest, suggesting irregularities in the washcoating process, likely due to adhesion issues. Instead, ceramic OCFs exhibit a uniform distribution of Co and Pd, as indicated by their consistent surface composition. Additionally, the analysis reveals the presence of elements inherent to the OCF material itself, in agreement with XRD analysis.

The H_2-TPR profiles for the coated OCFs, displayed in Figure 3A, were obtained at a heating rate of 10°C min^{-1}. The reduction process is marked by two distinct peaks: the first, occurring between 120 and 230°C, corresponds to the reduction of Co^{+3} to

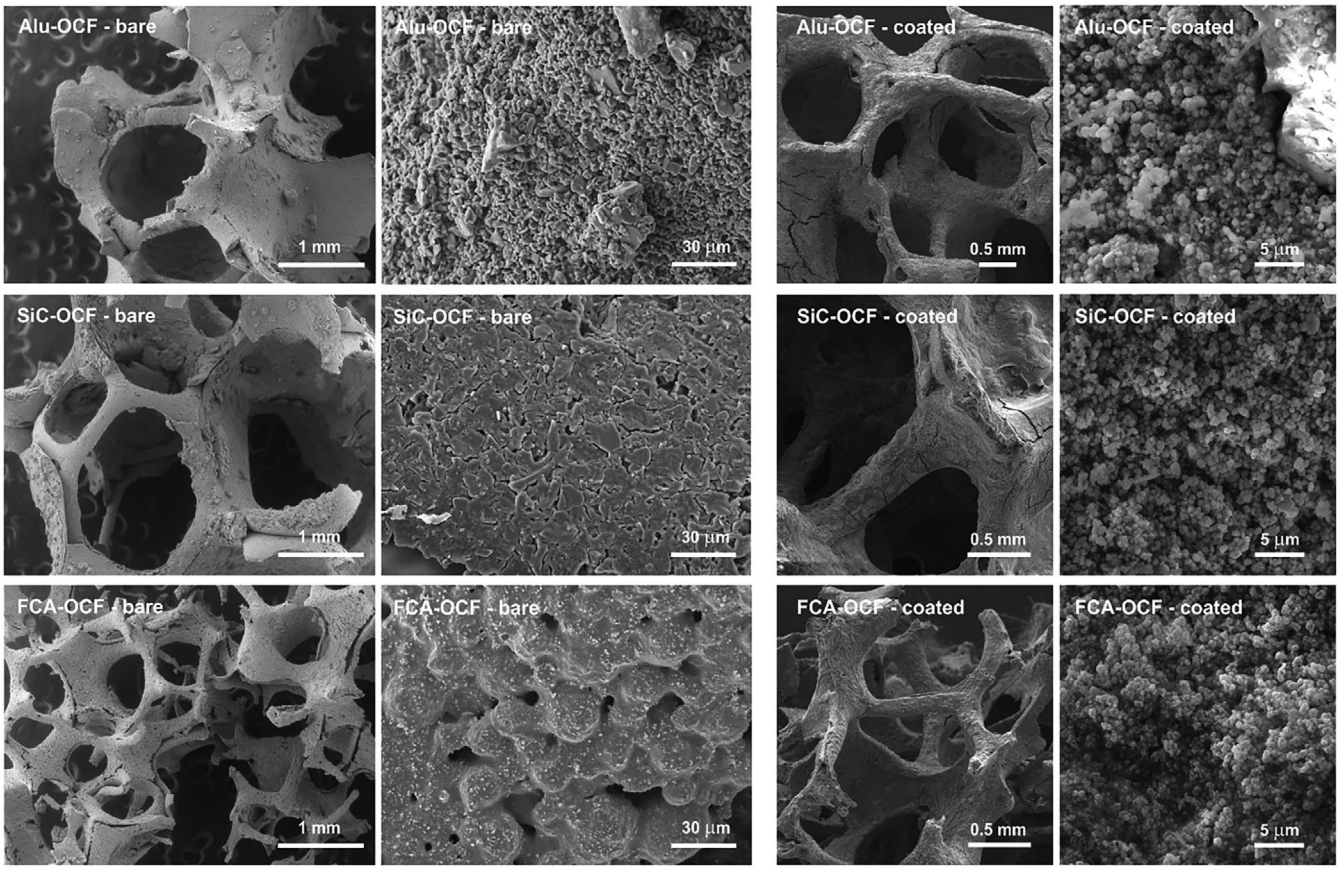

FIGURE 2 | FESEM and SEM images of all bare and coated OCFs.

TABLE 2 | XRF data analysis of PdO/Co_3O_4 on all coated OCFs.

Catalyst –OCF(PdO/Co_3O_4)	Compound	m/m %	Std.Err.	El.	m/m %	Std.Err.
Alu-OCF	Al_2O_3	59.0	1.0	Al	31.3	0.5
	Co_3O_4	25.3	0.3	Co	18.4	0.2
	SiO_2	10.2	0.65	Si	4.7	0.3
	PdO	3.07	0.1	Pd	2.6	0.1
	ZrO_2	1.78	0.1	Zr	1.3	0.1
SiC-OCF	SiC	62.8	0.5	Si	33.4	0.2
	Co_3O_4	25.3	0.2	Co	14.1	0.1
	Al_2O_3	8.5	0.6	Al	3.4	0.3
	PdO	2.4	0.1	Pd	1.6	0.1
	ZrO_2	1.0	0.1	Zr	0.6	0.1
FCA-OCF	Fe_2O_3	43.8	0.3	Fe	30.4	0.2
	Al_2O_3	26.3	0.5	Al	13.8	0.3
	Cr_2O_3	16.8	0.3	Cr	11.4	0.2
	Co_3O_4	12.0	0.2	Co	8.7	0.1
	MnO	0.8	0.2	Mn	0.6	0.1
	PdO	0.4	0.1	Pd	0.3	0.1

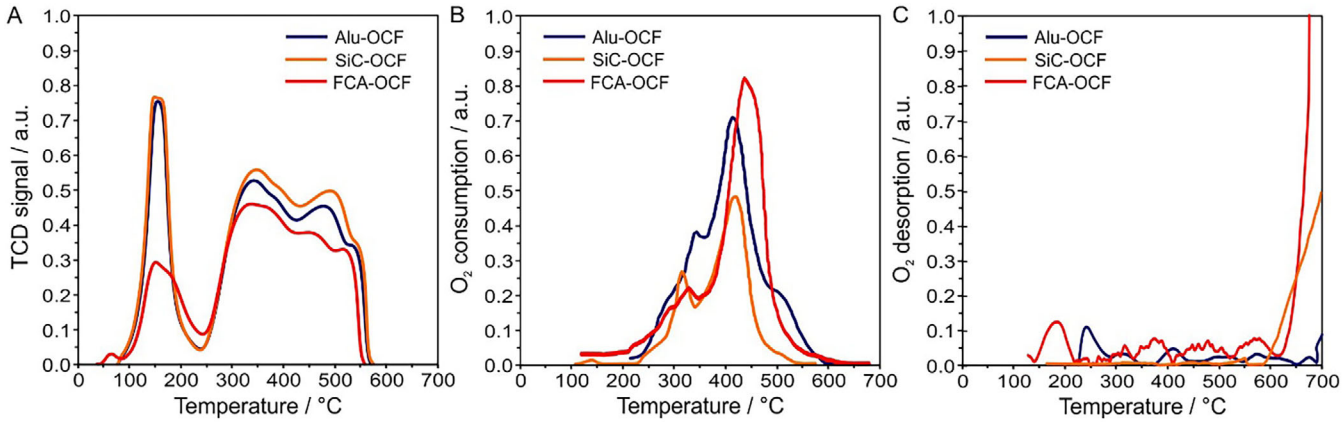

FIGURE 3 | (A) H_2-TPR (measured at 10°C min^{-1}), (B) O_2-TPO, and (C) O_2-TPD comparison of all coated OCFs.

TABLE 3 | XPS data analysis for all coated OCFs.

Catalyst –OCF(PdO/Co_3O_4)	Alu–OCF	SiC–OCF	FCA–OCF
Co 2p	6.2%	5.4%	15.3%
O 1s	64.1%	60.4%	61.0%
Pd 3d	2.2%	2.4%	0.7%
Al 2p	27.6%	14.4%	23.0%
Si 2p	—	16.0%	—
Pd/Co	0.35	0.44	0.05

Co^{+2}, and the second, appearing at temperatures above 500°C, corresponds to the reduction of Co^{+2} to CoO. The relative hydrogen consumption across the PdO/Co_3O_4 coated OCFs remains consistent, despite the known influence of particle size on reduction temperatures, where smaller particles typically reduce at lower temperatures [65, 66]. It is worth noting that oxide species originating from the FCA-OCF may promote the formation or stabilization of smaller PdO crystallites. As stated earlier, in the foams examined, the coating appears with few cracks, that could facilitate accessibility of the gas phase to the inner substrate. This effect could facilitate earlier redox activation of surface oxygen species, thanks to FeCr species, and may be reflected in the lower ignition temperatures observed in the corresponding light-off curves of FCA-OCF. This phenomenon, instead, is not visible in the other two foams, since neither SiO_2 nor Al_2O_3 contributes to the reduction peaks. Additionally, no hydrogen uptake was observed above 700°C, indicating the absence of other reducible phases in the samples. The characteristic peak for Pd oxide reduction was inconsistently observed, likely due to the low Pd content and high Co_3O_4/Pd ratio, resulting in minimal hydrogen consumption by Pd oxide relative to other metal oxides. Notably, the highest reduction was recorded for the PdO/Co_3O_4-coated Alu-OCF and SiC-OCF, suggesting greater availability of active oxygen on their surfaces.

While the support may influence catalyst reduction, the activation energy for Co_3O_4 reduction was determined from the slope of $\ln(\beta/T_{max})$ versus T^{-1}, providing results 43 kJ mol^{-1} for Alu- and FCA-OCF, and 44 kJ mol^{-1} for SiC-OCF. These results show no significant impact from the OCFs, as reduction energies remained similar across all structures. This analysis was based on a series of H_2-TPR measurements at varying heating rates (β = 5, 7.5, 10, 12.5, 15°C min^{-1}) followed by determining the corresponding temperature peaks.

Following a pre-reduction treatment, an O_2-TPO analysis was performed to assess the reoxidation capacity of the catalysts after complete reduction. The resulting profiles, illustrated in Figure 3B, revealed a prominent oxidation peak at 400-430°C and a smaller peak at 300°C–330°C. The intensity of the main oxidation peak increased with higher surface Co content across all coated OCFs, suggesting a greater propensity for oxidation with increased cobalt loading. The oxidation process commenced between 200°C–250°C and concluded around 600°C in all cases. Notably, the Pd/Co_3O_4 SiC-OCF exhibited a slightly earlier end to the oxidation process, indicating a faster reoxidation. This observation suggests that the support material has minimal impact on the oxidation process.

To explore the desorption behavior of different oxygen species from the coated OCFs and to evaluate the impact of gas-phase oxygen, O_2-TPD profiles were performed (Figure 3C). The typical desorption sequence for oxygen species is $O_2(ad) \rightarrow O_2^-(ad) \rightarrow O^-(ad) \rightarrow O^{2-}(_{latt})$ [67, 68]. In the absence of reducing gases, desorption in He occurs above 600°C and is attributed to bulk lattice oxygen (O_{latt}). The desorption peak temperatures for O_{latt} in all samples were notably lower than the reported value for pure Co_3O_4 (884°C) [69], suggesting that the inclusion of Pd enhances the mobility of O_{latt}. Lower desorption temperatures and higher quantities of desorbed lattice oxygen indicate improved lattice oxygen activity, facilitating its rapid removal and replenishment in line with the Mars-van Krevelen (M-v-K) mechanism. Notably, the FCA-OCF and SiC-OCF catalysts demonstrated superior lattice oxygen mobility and efficiency in breaking C—H bonds. Signals with magnitudes below 0.1 were considered instrumental noise and excluded from the analysis.

3.2 | Catalytic Performance in Dry and Wet Environments

The study focused on the effects of water inhibition on thermally aged coated OCFs under steady-state conditions, using 1 vol.% CH_4 at a WHSV of 30 NmL h^{-1} $g_{cat}{}^{-1}$. The structured catalysts were subjected to ignition and extinction tests by introducing

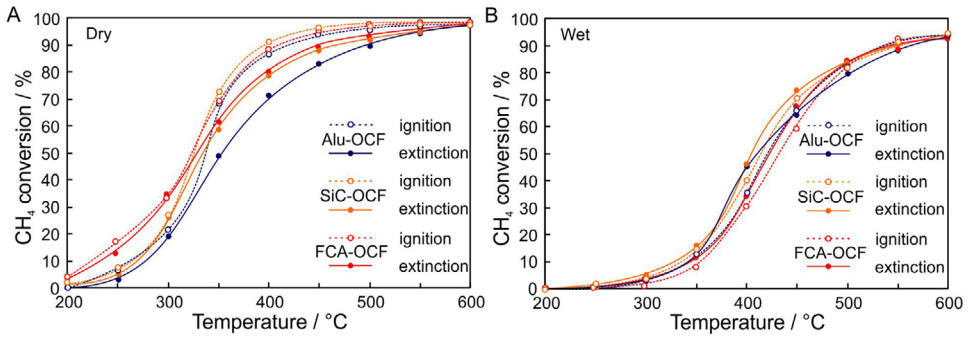

FIGURE 4 | Comparison of dry (A) and wet (B) conversions over PdO/Co_3O_4-coated OCFs.

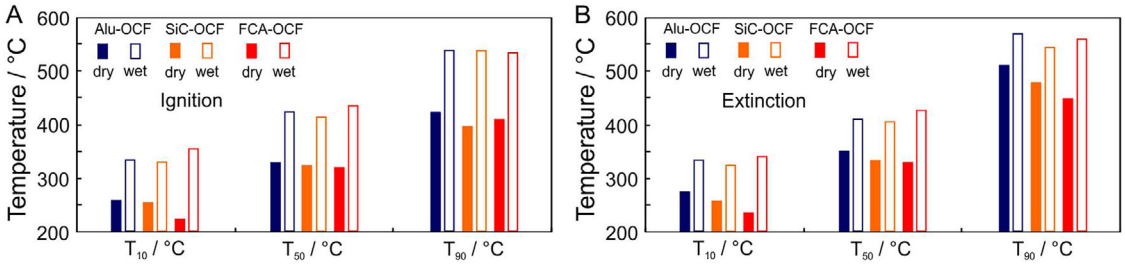

FIGURE 5 | Ignition (A) and Extinction (B) T_{10}, T_{50}, and T_{90} over PdO/Co_3O_4-coated OCFs in dry and wet conditions.

10 vol.% H_2O into the inlet feed, setting a temperature range of 200°C–600°C. Water-induced deactivation was observed, producing a decline in conversions compared to those in dry conditions. Figure 4 presents a comparative analysis of ignition and extinction curves under both dry and wet conditions. In dry conditions, a slight hysteresis between the curves at elevated temperatures is noted in certain cases. However, under wet conditions, the hysteresis is either significantly reduced or entirely absent in most samples, suggesting that the presence of water alters the chemical environment on the catalyst surface. A comparison across all structures reveals a noticeable decline in the performance of both ceramic and metallic OCFs when water is introduced. This phenomenon is clearly demonstrated by analyzing the T_{10}, T_{50}, and T_{90} values from the ignition and extinction curves (Figure 5). The data reveal a striking similarity across all structures, particularly under wet conditions, suggesting no substantial performance differences between the various OCFs.

Figure 6 illustrates the Arrhenius plots for the catalytic structures evaluated over a temperature range of 200°C–600°C in both dry and wet conditions. The nearly parallel slopes, characterized by $(-E_a/R_g)$, suggest similar apparent activation energies across the different systems. The influence of water is visible, as the curves shift to higher temperatures and significantly lower reaction constants. At higher temperatures, the reaction rate increases, reducing resistance and amplifying the significance of diffusional effects. This is evidenced by changes in the slope $(-E_{app}/R_g)$ of the Arrhenius plots with varying temperatures. At intermediate temperatures, the slope decreases to approximately half of the value observed in the kinetic regime ($E_a \approx E_{app}/2$), indicating the growing impact of internal diffusion limitations. At very high temperatures, the slope approaches zero, signifying that external diffusion effects dominate ($E_a \approx 0$), further highlighting the transition from kinetic to transport-limited regimes.

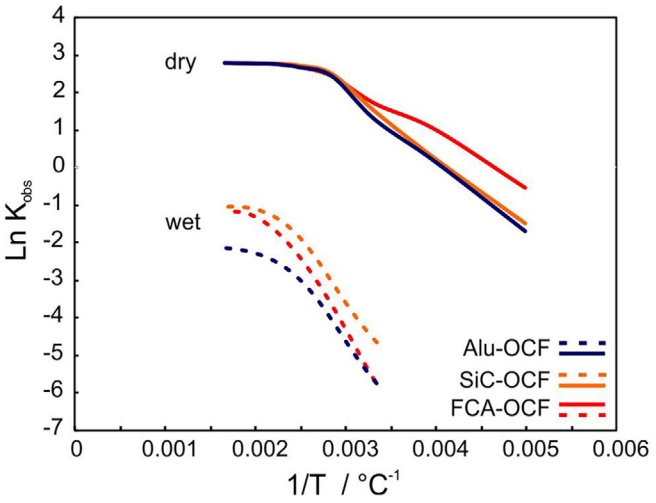

FIGURE 6 | Arrhenius plots computed with MATLAB for all the coated OCFs in dry and 10 vol% H_2O environment at WHSV of 30 and inlet CH_4 concentration of 1 wt%. Kinetic data computed only for conversion values below 15%.

3.3 | Hydrothermal Stability

Continued water exposure is recognized as a key factor in the irreversible deactivation of catalysts. It is associated with the presence of inactive $Pd(OH)_2$ as a primary cause, which suppresses oxygen exchange between the support and Pd active sites, leading to diminished catalyst activity [70]. This deactivation mechanism predominantly operates below 450°C, whereas at temperatures above 500°C, water-assisted sintering of Pd catalysts becomes significant. In lean-burn CH_4 oxidation, oxygen molecules dissociate on Pd^{-}* sites and exchange with oxygen from the support,

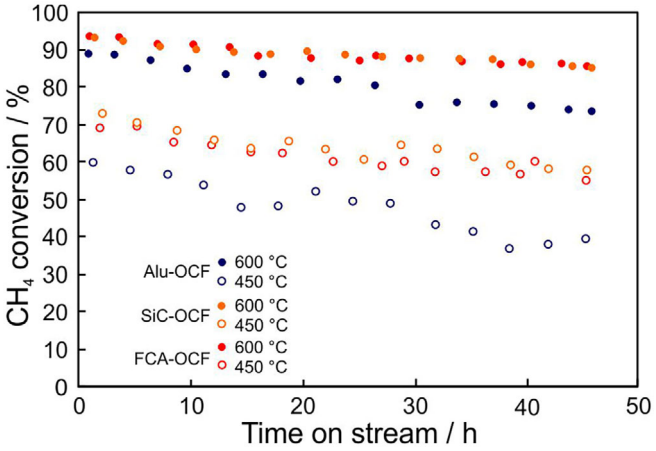

FIGURE 7 | Hydrothermal aging during 45 h with 10 vol.% H_2O of different PdO/Co_3O_4 coated OCFs.

enabling the re-oxidation of Pd during the reaction. However, hydroxyl groups, which tend to migrate to the oxide support rather than desorb, disrupt this oxygen exchange by increasing OH coverage as water dissociates. This leads to a reduction in active PdO sites over time, thereby decreasing CH_4 conversion [12]. The oxygen concentration in the reaction environment thus plays a critical role in maintaining catalytic performance. To counteract deactivation caused by water, especially below 450°C, it is essential to use a catalytic support with high oxygen surface mobility [71]. It has been demonstrated that the choice of support material, along with its inherent oxygen mobility, plays a crucial role in slowing down catalyst deactivation and significantly enhancing resistance to water-induced deactivation.

In this study, the stability of coated SiC, Alu, and FCA structures was evaluated through hydrothermal aging (HTA), exposing them to a $CH_4/O_2/N_2$ feed containing 1 vol% CH_4 and 10 vol% H_2O at 30 NmL h^{-1} $g_{cat}{}^{-1}$ WHSV for 45 h, with temperature cycling between 450°C and 600°C (Figure 7). This experiment was designed to test the hydrothermal resistance of the OCFs at both high and intermediate temperatures. The results indicated that all structures maintained good stability overall. The sustained catalytic activity at elevated temperatures is likely due to the strong resistance of the OCFs to sintering. However, a more noticeable decline in methane conversion was observed at the lower temperature of 450°C (Table S1). The coated Alu-OCF exhibited the lowest stability, showing the most significant reduction in conversion throughout the measurement period. While both SiC-OCF and FCA-OCF displayed a highly stable behavior.

The focus of our investigation centres on catalytic systems on Pd over cobalt oxide catalysts, deposited on various material supports. Although those supports have essentially structural functions, they cannot be discarded as having potential interactions with the catalysts themselves. These interactions may impact not only heat and mass transfer issues but also the susceptibility to water poisoning. Alumina is characterized by low thermal stability, exacerbating degradation processes, particularly under the influence of water, due to the lower oxygen mobility compared to the other supports [12, 72], even if in the examined temperature range it should be stable. Previous studies on Pd/OAl_2O_3 also revealed a strong enthalpy of H_2O adsorption, suggesting that the diminished activity of PdO/Al_2O_3 in the presence of H_2O results from a high coverage of active sites by H_2O [9, 10, 73]. The accumulation of hydroxyl groups on the support impedes oxygen migration and exchange, thereby affecting CH_4 oxidation. Consequently, the strong adsorption of H_2O aligns with high hydroxyl accumulation on the catalyst surface, inhibiting O exchange.

3.4 | Kinetic Study of the Coated OCFs

Kinetic studies were performed after the catalysts were deactivated by HTA. To minimize the influence of ongoing deactivation, multiple repetitive experiments were conducted to ensure consistency. Apparent activation energies were determined at 10% conversion using a differential packed-bed reactor concept. Nonlinear optimization and numerical analysis were performed using MATLAB code. Ignition curves were generated from reproducible runs with varying initial CH_4 concentrations (1%, 0.8%, 0.5%, and 0.3%) in both dry and wet conditions, allowing for the assessment of methane reaction order under these different environments. Additionally, varying initial H_2O concentrations (8%, 5%, and 3%) were tested to evaluate the impact of water on each OCF. Across all experiments, fractional conversion remained independent of CH_4 concentration, indicating a first-order dependency on CH_4. Parity plots (Figure 8) compared experimental and predicted conversions, incorporating ±15% error lines to validate the obtained results. The absence of external and internal mass transfer was confirmed using Carberry and Weisz-Prater numbers, while Mears and Anderson criteria were applied to ensure the absence of external and internal heat transfer limitations. The analysis of reaction rates and activation energies from the modeling confirmed that there were no significant transport limitations, being all the computed Ca, WP, Mears and Anderson values well below the limits (Table S2).

4 | Discussion

Throughout the study of catalytic methane combustion, SiC-, Alu-, and FCA-OCFs were examined. However, to the best of our knowledge, the kinetic study on catalytic foams is limited to SiC foam, which has shown stable catalytic performance with no significant structural changes detected [74]. In this work, methane combustion follows a first-order reaction across all cases, while the reaction order concerning water varies, highlighting the role of the support in influencing the reaction. Specifically, the water order is −0.9 for Alu-OCF, −0.7 for SiC-OCF and FCA-OCF (Table 4). Despite these differences, the activation energy remains consistent for all three supports under both dry and wet conditions, measuring 117 kJ mol^{-1} in dry and 129 kJ mol^{-1} in wet environments. Although the activation energy is similar across the studied materials, the pre-exponential factor (k_0) shows significant variation, reflecting the differences in active site concentration due to different interactions between the active phase and the support [72]. Under dry conditions, the pre-exponential factor follows the order SiC > Alu > FCA, while under wet conditions, the order shifts to Alu > SiC > FCA, with a marked decrease in values, particularly for FCA-OCF, suggesting potential active site blockage under wet conditions. The variation in water order indicates that the Alu-OCF structure

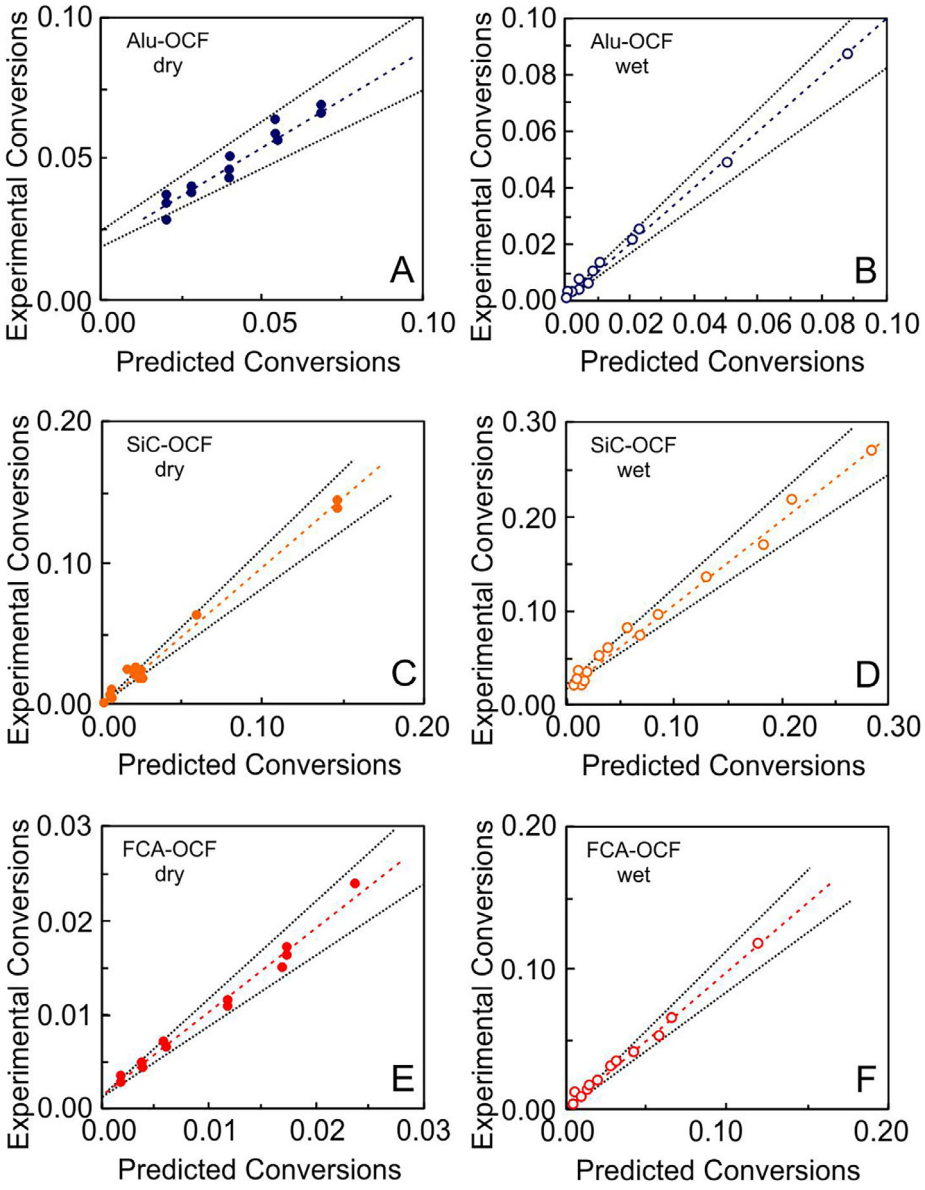

FIGURE 8 | Parity plot comparing experimental and predicted dry (left) and wet (right) conversions in different PdO/Co_3O_4 coated OCFs for data validation with ±15% error lines (A) Al-OCF (B) FeCrAl-OCF (C) SiC-OCF.

TABLE 4 | Calculated kinetic parameters of different PdO/Co_3O_4 coated OCFs.

Catalyst OCF(PdO/Co_3O_4)		Water order	E_a kJ mol^{-1}	k_0 m^3 kg^{-1} s^{-1}
Alu-OCF	Dry	—	117.2	24,046
	Wet	−0.9	129.7	19,487
SiC-OCF	Dry	—	117.2	26,894
	Wet	—0.7	128.7	10,842
FCA-OCF	Dry	—	117.2	21,244
	Wet	−0.7	128.4	3,863

is more sensitive to the presence of water than SiC-OCF and FCA-OCF. Additionally, the hydrophobicity of the support appears to influence the degree of water inhibition, with SiC-OCF being the most hydrophobic of the structures analyzed [71].

The PdO dispersion data from CO chemisorption, measured again at the end of catalytic tests (Table 5), were employed to calculate TOF values by normalizing the reaction rate by the estimated number of superficial metallic atoms. The observed differences in metal dispersion among the various OCF-supported catalysts arise from a combination of metal–support interactions and preparation history. In particular, the washcoating process may lead to nonuniform catalyst layers with different effective thicknesses and local Pd concentrations depending on the OCF type. In addition, the foam material (metallic or ceramic, with different values of thermal conductivities) can influence the thermal stability of the catalyst during calcination, resulting in different apparent dispersions after coating and cracking of the surface of the catalytic layer. Moreover, although Co_3O_4 is

TABLE 5 | Calculated TOF values based on metal dispersion (re-evaluated after HTA) at dry (300°C) and wet (375°C) conditions, and 0.5% CH_4.

Catalyst OCF(PdO/Co_3O_4)	Metal dispersion (%)		Reaction rate kmol kg^{-1} s^{-1}	Rate constant s^{-1}	Apparent CH_4 TOF s^{-1}
Alu-OCF	0.89	Dry	1.39E−04	1.643	0.028
		Wet	1.08E−04	0.022	0.021
SiC-OCF	2.05	Dry	7.37E−05	0.780	0.006
		Wet	9.15E−05	0.001	0.008
FCA-OCF	10.24	Dry	6.18E−05	0.652	0.001
		Wet	2.60E−05	0.001	0.001

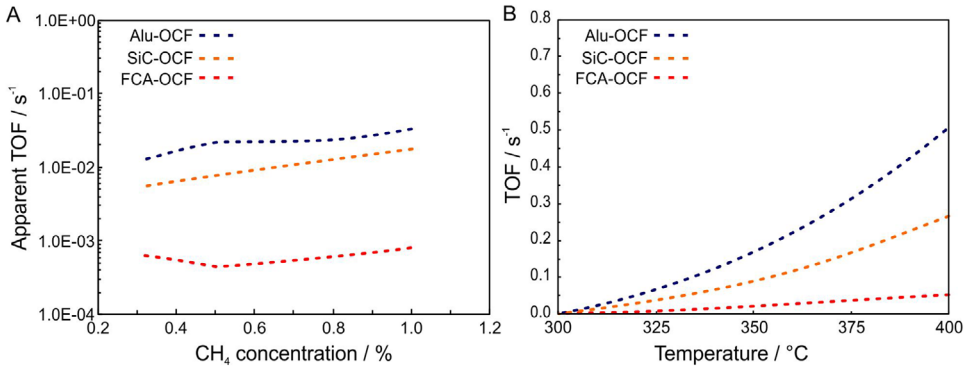

FIGURE 9 | Comparison of the calculated apparent TOFs under 10 vol% H_2O at 375°C conditions and various CH_4 concentrations over coated OCFs (A); comparison of the calculated apparent TOFs in the temperature range of 300°C to 600°C over coated OCFs at 1 vol% CH_4 and 10 vol% H_2O (B).

catalytically active in wet methane combustion, the apparent TOF was intentionally calculated based solely on Pd dispersion for all catalysts to ensure a consistent normalization basis. TOF values were calculated at 375°C for wet conditions, using varying initial CH_4 concentrations (0.3%–1%) with 10 vol% H_2O (Table 5). Under the tested water vapor concentration, the catalysts operate in a regime where overall reaction rates are largely governed by macroscopic or transport-related effects rather than by intrinsic differences in Pd site activity. Consequently, the apparent TOF comparison is not intended to demonstrate superior water tolerance, but rather to evaluate whether Pd utilization efficiency varies with OCF type under identical wet conditions and to verify that no severe deactivation or loss of accessible Pd sites occurs in the presence of water vapor. The observed increase in TOF with rising methane concentrations (Figure 9) suggests enhanced catalytic efficiency, likely due to greater coverage of active sites by methane molecules, increasing the likelihood of successful catalytic reactions. Although the coated FCA-OCF exhibits the lowest TOF values, the Alu-OCF-based structure demonstrates superior TOF across various CH_4 concentrations and the entire temperature range tested (Figure 9). Despite having the lowest metal dispersion, the Alu-OCF structure effectively utilizes its active sites, achieving significant reaction rates.

Reaction rates were evaluated for all catalyst structures under both dry and wet conditions (Figure 10A). The data reveal that, overall, the supports exhibit similar reaction rates, with SiC-OCF demonstrating consistently slightly better performance in both conditions. This trend is further supported by the increase in reaction rates across a range of operational temperatures (Figure 10B). The results indicate that the coated FCA-OCF exhibits the slowest reaction rate, whereas the coated SiC-OCF demonstrates the highest rates across all tested temperatures. Notably, FCA-OCF exhibited greater compositional variation, indicating potential issues with coating adhesion, which may have contributed to its increased sensitivity to water-induced deactivation. These findings suggest that metallic foams, particularly FCA-OCF, require tailored pretreatment to ensure uniform and stable washcoating.

5 | Conclusions

This study investigated the effects of water inhibition on thermally aged, coated open-cell foams (OCFs) under steady-state conditions for wet lean methane combustion. SiC-, FeCrAlloy-, and alumina OCFs were washcoated with PdO/Co_3O_4 catalyst, and their performance was assessed in the absence and presence of 10 vol% of water. The introduction of water into the feed stream significantly reduced catalytic activity, requiring higher temperatures to achieve comparable conversion rates to dry conditions. Wet conditions also diminished or eliminated hysteresis in the ignition and extinction curves, suggesting altered surface chemistry on the catalysts.

Kinetic studies, performed under differential conditions following hydrothermal aging, confirmed a first-order dependency on methane for all catalytic systems. Both external and internal transport limitations were found to be absent. Water presence significantly impacted methane conversion, with higher water concentrations leading to reduced reaction rates. The increase in

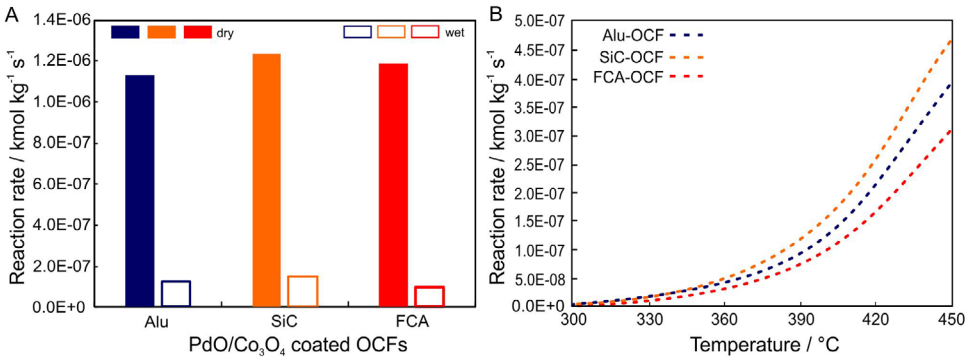

FIGURE 10 | (A) Reaction rate in dry and 10 vol% H_2O at 400°C, 1 vol% CH_4, and 30 WHSV of OCFs coated with PdO/Co_3O_4 catalysts. (B) Reaction rates in the range of temperatures in which the kinetic regime is dominant at 1 vol% CH_4 and 10 vol% H_2O for the three coated OCFs.

apparent activation energies under wet conditions is attributed to water adsorption on the catalyst surface, which inhibits methane activation and raises the energy required for water desorption.

Further analysis of the catalyst supports revealed different degrees of water inhibition among coated SiC-, Alu-, and FCA-OCFs. Although the support material had no effect on the activation energy, as expected with the same active site, it influenced the water order and pre-exponential factor. SiC-OCF exhibited the least negative water order, while FCA-OCF experienced the greatest reduction in the pre-exponential factor, potentially due to active site blockage under wet conditions, resulting in lower TOF values. The hydrophobicity of the supports appeared to play a role in water inhibition, with SiC-OCF, the most hydrophobic of the materials tested, demonstrating superior catalytic activity.

Acknowledgments

H.G.M. acknowledges Politecnico di Torino for the scholarship to visit University of Alberta and Jagiellonian University.

Open access publishing facilitated by Politecnico di Torino, as part of the Wiley - CRUI-CARE agreement.

Conflicts of Interest

The authors declare no conflicts of interest.

Data Availability Statement

The data that support the findings of this study are available from the corresponding author upon reasonable request.

References

1. D. Shindell, F. Bréon, W. Collins, et al., *Anthropogenic and Natural Radiative Forcing. In: Climate Change 2013: The Physical Science Basis*, ed. T.F. Stocker, G.-K.P. D. Qin, M. Tignor, S.K. Allen, A. J. Boschung, Y. Nauels (Cambridge University Press, 2013): 659–730.

2. R. O. Yusuf, Z. Z. Noor, A. H. Abba, M. A. A. Hassan, and M. F. M. Din, "Methane Emission by Sectors: A Comprehensive Review of Emission Sources and Mitigation Methods," *Renewable and Sustainable Energy Reviews* 16 (2012): 5059–5070, https://doi.org/10.1016/j.rser.2012.04.008.

3. M. A. Mac Kinnon, J. Brouwer, and S. Samuelsen, "The Role of Natural Gas and Its Infrastructure in Mitigating Greenhouse Gas Emissions, Improving Regional Air Quality, and Renewable Resource Integration," *Progress in Energy and Combustion Science* 64 (2018): 62–92, https://doi.org/10.1016/j.pecs.2017.10.002.

4. P. Lott, M. Casapu, J. D. Grunwaldt, and O. Deutschmann, "A Review on Exhaust Gas After-Treatment of Lean-Burn Natural Gas Engines—From Fundamentals to Application," *Applied Catalysis B: Environment and Energy* 2024, 340, 123241, https://doi.org/10.1016/j.apcatb.2023.123241.

5. M. Monai, T. Montini, R. J. Gorte, and P. Fornasiero, "Catalytic Oxidation of Methane: Pd and Beyond," *European Journal of Inorganic Chemistry* 2018 (2018): 2884–2893, https://doi.org/10.1002/ejic.201800326.

6. E. Akbari, S. M. Alavi, M. Rezaei, and A. Larimi, "Preparation and Evaluation of A/ BaO-MnO_X Catalysts (A: Rh, Pt, Pd, Ru) in Lean Methane Catalytic Combustion at Low Temperature," *International Journal of Energy Research* 46 (2022): 6292–6313, https://doi.org/10.1002/er.7567.

7. J. M. Jones, V. A. Dupont, R. Brydson, et al., "Sulphur Poisoning and Regeneration of Precious Metal Catalysed Methane Combustion," *Catalysis Today* 81 (2003): 589–601, https://doi.org/10.1016/S0920-5861(03)00157-3.

8. L. S. Escandón, S. Ordóñez, A. Vega, and F. V. Díez, "Sulphur Poisoning of Palladium Catalysts Used for Methane Combustion: Effect of the Support," *Journal of Hazardous Materials* 153 (2008): 742–750, https://doi.org/10.1016/j.jhazmat.2007.09.017.

9. R. Gholami, M. Alyani, and K. J. Smith, "Deactivation of Pd Catalysts by Water During Low Temperature Methane Oxidation Relevant to Natural Gas Vehicle Converters," *Catalysts* 5 (2015): 561–594, https://doi.org/10.3390/catal5020561.

10. R. S. Kumar, R. E. Hayes, and N. Semagina, "Pd and Pd-Pt Catalysts Supported on SnO_2 and γ-Al_2O_3: Kinetic Studies of Wet Lean Methane Combustion," *Chemical Engineering Journal* 269 (2023): 118488, https://doi.org/10.1016/j.ces.2023.118488.

11. M. Zanoletti, F. Godard, and M. Perrier, "Effect of Support on the Apparent Activity of Palladium Oxide in Catalytic Methane Combustion," *Canadian Journal of Chemical Engineering* 98 (2020): 2205–2213, https://doi.org/10.1002/cjce.23734.

12. W. R. Schwartz, D. Ciuparu, and L. D. Pfefferle, "Combustion of Methane Over Palladium-Based Catalysts: Catalytic Deactivation and Role of the Support," *Journal of Physical Chemistry C* 116 (2012): 8587–8593, https://doi.org/10.1021/jp212236e.

13. J. Chen, H. Arandiyan, X. Gao, and J. Li, "Recent Advances in Catalysts for Methane Combustion," *Catalysis Surveys from Asia* 19 (2015): 140–171, https://doi.org/10.1007/s10563-015-9191-5.

14. Z. Ma, "Cobalt Oxide Catalysts for Environmental Remediation," *Current Catalysis* 3 (2014): 15–26, https://doi.org/10.2174/2211544711302999017.

15. X. Zhang, X. Jin, L. Bao, et al., "Construction of Defective Cobalt Oxide for Methane Combustion by Oxygen Vacancy Engineering," *New Journal of Chemistry* 45 (2021): 12655–12660, https://doi.org/10.1039/d1nj01296g.

16. J. Chen, X. Wu, and A. Selloni, "Electronic Structure and Bonding Properties of Cobalt Oxide in the Spinel Structure," *Physical Review B* 83 (2011): 245204, https://doi.org/10.1103/PhysRevB.83.245204.

17. S. Nasr, N. Semagina, and R. E. Hayes, "Kinetic Modelling of Co_3O_4- and Pd/Co_3O_4-Catalyzed Wet Lean Methane Combustion," *Emission Control Science and Technology* 6 (2020): 269–278, https://doi.org/10.1007/s40825-019-00143-0.

18. V. Tomašić and F. Jović, "State-Of-The-Art in the Monolithic Catalysts/Reactors," *Applied Catalysis A: General* 311 (2006): 112–121, https://doi.org/10.1016/j.apcata.2006.06.013.

19. A. Cybulski and J. Moulin, "Monoliths in Heterogeneous Catalysis," *Catalysis Reviews* 36 (1994): 179–270, https://doi.org/10.1080/01614949408013925.

20. J. W. Geus and J. C. Van Giezen, "Monoliths in Catalytic Oxidation," *Catalysis Today* 47 (1999): 169–180, https://doi.org/10.1016/S0920-5861(98)00297-1.

21. A. Aguirre, V. Chandra, E. A. J. F. Peters, J. A. M. Kuipers, and M. F. Neira D'Angelo, "Open-Cell Foams as Catalysts Support: A Systematic Analysis of the Mass Transfer Limitations," *Chemical Engineering Journal* 393 (2020): 124656, https://doi.org/10.1016/j.cej.2020.124656.

22. P. H. Ho, M. Ambrosetti, G. Groppi, et al., "Structured Catalysts-Based on Open-Cell Metallic Foams for Energy and Environmental Applications," *Studies in Surface Science and Catalysis* 178 (2019): 303–327, https://doi.org/10.1016/B978-0-444-64127-4.00015-X.

23. M. De Paepe, P. Huisseune, P. De Jaeger, and C. Joen, "The Use of Open Cell Metal Foams in Heat Exchangers: Possibilities and Limitations", in *8th International Conference on Heat Transfer* (Fluid Mechanics and Thermodynamics, 2011): 1–15.

24. R. Coquard, M. Loretz, and D. Baillis, "Conductive Heat Transfer in Metallic/Ceramic Open-Cell Foams," *Advanced Engineering Materials* 10 (2008): 323–337, https://doi.org/10.1002/adem.200700331.

25. A. Muley, C. Kiser, B. Sundén, and R. K. Shah, "Foam Heat Exchangers: A Technology Assessment," *Heat Transfer Engineering* 33 (2012): 42–51, https://doi.org/10.1080/01457632.2011.584817.

26. G. Contento, M. Iasiello, M. Oliviero, N. Bianco, and V. Naso, "Morphology of Open-Cell Foams: A Critical Review and Geometric Modeling," *Journal of Porous Media* 22 (2019): 869–887, https://doi.org/10.1615/JPorMedia.2019028906.

27. A. August and B. Nestler, "About the Surface Area to Volume Relations of Open Cell Foams," *Engineering Research Express* 2 (2020): 015021, https://doi.org/10.1088/2631-8695/ab6ac6.

28. A. Aguirre, E. Scholman, J. van der Shaaf, and M. F. Neira d'Angelo, "Controlling the Selectivity in the Fischer-Tropsch Synthesis Using Foam Catalysts: An Integrated Experimental and Modeling Approach," *Chemical Engineering Journal* 409 (2021): 128139, https://doi.org/10.1016/j.cej.2020.128139.

29. E. Meloni, M. Caldera, V. Palma, V. Pignatelli, and V. Gerardi, "Soot Abatement From Biomass Boilers by Means of Open-Cell Foams Filters," *Renewable Energy* 131 (2019): 745–754, https://doi.org/10.1016/j.renene.2018.07.098.

30. A. Klegova, A. Inayat, P. Indyka, et al., "Cobalt Mixed Oxides Deposited on the SiC Open-Cell Foams for Nitrous Oxide Decomposition," *Applied Catalysis B: Environmental* 255 (2019): 117745, https://doi.org/10.1016/j.apcatb.2019.117745.

31. F. C. Patcas, G. I. Garrido, and B. Kraushaar-Czarnetzki, "CO Oxidation Over Structured Carriers: A Comparison of Ceramic Foams, Honeycombs and Beads," *Chemical Engineering Science* 62 (2007): 3984–3990, https://doi.org/10.1016/j.ces.2007.04.039.

32. P. Surmacz and Z. Gut, "The Experimental Investigation of a 98% Hydrogen Peroxide Monopropellant Thruster Comprising the Metal-Foam-Supported Manganese Oxide Catalyst," *Aerospace* 10 (2023): 215, https://doi.org/10.3390/aerospace10030215.

33. B. Ozmat, B. Leyda, and B. Benson, "Thermal Applications of Open-Cell Metal Foams," in *Materials and Manufacturing Processes* (Marcel Dekker Inc., 2004): 839–862, https://doi.org/10.1081/AMP-200030568.

34. W. M. Carty and P. W. Lednor, "Monolithic Ceramics and Heterogeneous Catalysts: Honeycombs and Foams," *Current Opinion in Solid State and Materials Science* 1 (1996): 88–95, https://doi.org/10.1016/S1359-0286(96)80015-5.

35. C. W. Moncada Quintero, H. G. Mazzei, M. Servel, et al., "Investigating Mass Transfer Coefficients in Lean Methane Combustion Reaction Through the Morphological and Geometric Analysis of Structured Open Cell Foam Catalysts," *Chemical Engineering Science* 281 (2023): 119138, https://doi.org/10.1016/j.ces.2023.119138.

36. F. Kapteijn and J. A. Moulijn, "Structured Catalysts and Reactors—Perspectives for Demanding Applications," *Catalysis Today* 383 (2020): 5–14, https://doi.org/10.1016/j.cattod.2020.09.026.

37. S. A. Solovev, O. V. Soloveva, I. G. Akhmetova, Y. V. Vankov, and D. L. Paluku, "Numerical Simulation of Heat and Mass Transfer in an Open-Cell Foam Catalyst on Example of the Acetylene Hydrogenation Reaction," *Chemical Engineering Journal* 6 (2022): 11, https://doi.org/10.3390/chemengineering6010011.

38. H. Chen, Y. Shao, Y. Mu, et al., "Structured Silicalite-1 Encapsulated Ni Catalyst Supported on SiC Foam for Dry Reforming of Methane," *American Institute of Chemical Engineers Journal* 67 (2021): e17126, https://doi.org/10.1002/aic.17126.

39. K. Pacultová, A. Klegova, T. Kiška, et al., "Effect of Support on the Catalytic Activity of Co_3O_4-Cs Deposited on Open-Cell Ceramic Foams for N_2O Decomposition," *Materials Research Bulletin* 129 (2020): 110892, https://doi.org/10.1016/j.materresbull.2020.110892.

40. L. M. Martínez Tejada, M. I. Domínguez, O. Sanz, M. A. Centeno, and J. A. Odriozola, "Au/CeO_2 Metallic Monolith Catalysts: Influence of the Metallic Substrate," *Gold Bulletin* 46 (2013): 221–231, https://doi.org/10.1007/s13404-013-0102-0.

41. R. Balzarotti, M. Ambrosetti, A. Beretta, G. Groppi, and E. Tronconi, "Investigation of Packed Conductive Foams as a Novel Reactor Configuration for Methane Steam Reforming," *Chemical Engineering Journal* 391 (2020): 123494, https://doi.org/10.1016/j.cej.2019.123494.

42. H. Yang, J. Li, H. Yu, F. Peng, and H. Wang, "Metal-Foam-Supported Pd/Al_2O_3 Catalysts for Catalytic Combustion of Methane: Effect of Interaction Between Support and Catalyst," *International Journal of Chemical Reactor Engineering* 13 (2015): 83–93, https://doi.org/10.1515/ijcre-2014-0009.

43. D. F. M. Santos, O. S. G. P. Soares, J. L. Figueiredo, O. Sanz, M. Montes, and M. F. R. Pereira, "Preparation of Ceramic and Metallic Monoliths Coated With Cryptomelane as Catalysts for VOC Abatement," *Chemical Engineering Journal* 382 (2020): 122923, https://doi.org/10.1016/j.cej.2019.122923.

44. J. M. Zamaro, M. A. Ulla, and E. E. Miró, "Growth of Mordenite on Monoliths by Secondary Synthesis," *Applied Catalysis A: General* 314 (2006): 101–113, https://doi.org/10.1016/j.apcata.2006.08.013.

45. K. Khivantsev, N. R. Jaegers, L. Kovarik, et al., "The Superior Hydrothermal Stability of Pd/SSZ-39 in Low Temperature Passive NOx Adsorption (PNA) and Methane Combustion," *Applied Catalysis B: Environmental* 280 (2021): 119449, https://doi.org/10.1016/j.apcatb.2020.119449.

46. J. Labuschagne, R. Meyer, Z. H. Chonco, J. M. Botha, and D. J. Moodley, "Application of Water-Tolerant Co/β-SiC Catalysts in Slurry Phase Fischer–Tropsch Synthesis," *Catalysis Today* 275 (2016): 2–10, https://doi.org/10.1016/j.cattod.2016.01.039.

47. Y. Zhao, Z. Gu, D. Li, et al., "Catalytic Combustion of Lean Methane Over $MnCo_2O_4$/SiC Catalysts: Enhanced Activity and Sulfur Resistance," *Fuel* 323 (2022): 124399, https://doi.org/10.1016/j.fuel.2022.124399.

48. Y. Guan, Y. Zhou, C. Jiang, et al., "Catalytic Combustion of Volatile Organic Compounds (VOCs) Over Structured Co_3O_4 Nano-Flowers on Silicalite-1/SiC Foam Catalysts," *Microporous and Mesoporous Materials* 323 (2021): 111173, https://doi.org/10.1016/j.micromeso.2021.111173.

49. D. Ugues, S. Specchia, and G. Saracco, "Optimal Microstructural Design of a Catalytic Premixed FeCrAlloy Fiber Burner for Methane Combustion," *Industrial & Engineering Chemistry Research* 43 (2004): 1990–1998, https://doi.org/10.1021/ie034202q.

50. G. Pauletto, A. Vaccari, G. Groppi, et al., "FeCrAl as a Catalyst Support," *Chemical Reviews* 120 (2020): 7516–7550, https://doi.org/10.1021/acs.chemrev.0c00149.

51. D. H. Kim, B. Y. Yu, P. R. Cha, W. Y. Yoon, J. Y. Byun, and S. H. Kim, "A Study on FeCrAl Foam as Effective Catalyst Support Under Thermal and Mechanical Stresses," *Surface and Coatings Technology* 209 (2012): 169–176, https://doi.org/10.1016/j.surfcoat.2012.08.017.

52. J. Jia, J. Zhou, C. Zhang, et al., "Preparation and Characterization of Ir-Based Catalysts on Metallic Supports for High-Temperature Steam Reforming of Methanol," *Applied Catalysis A: General* 341 (2008): 1–7, https://doi.org/10.1016/j.apcata.2007.11.006.

53. T. H. Lee, U. Jung, H. B. Im, et al., "Comparative Evaluation of Ru-Coated Fecralloy and SiC Monolithic Catalysts in Catalytic Partial Oxidation of Natural Gas for Hydrogen Production," *Journal of Industrial and Engineering Chemistry* 110 (2022): 178–187, https://doi.org/10.1016/j.jiec.2022.02.050.

54. R. V. Umretiya, W. Zhang, R. Motyl, et al., "Effect of Microstructure, Manufacturing Method and Composition on Corrosion Behavior of FeCrAl Alloys," in *Proceedings of TopFuel 2022 Light Water Reactor Fuel Performance Conference*, (American Nuclear Society, 2022): 228–235, https://doi.org/10.13182/TopFuel22-39013.

55. G. Ercolino, G. Grzybek, P. Stelmachowski, S. Specchia, A. Kotarba, and V. Specchia, "Pd/Co_3O_4-Based Catalysts Prepared by Solution Combustion Synthesis for Residual Methane Oxidation in Lean Conditions," *Catalysis Today* 257 (2015): 66–71, https://doi.org/10.1016/j.cattod.2015.03.006.

56. G. Ercolino, P. Stelmachowski, G. Grzybek, A. Kotarba, and S. Specchia, "Optimization of Pd Catalysts Supported on Co_3O_4 for Low-Temperature Lean Combustion of Residual Methane," *Applied Catalysis B: Environmental* 206 (2017): 712–725, https://doi.org/10.1016/j.apcatb.2017.01.055.

57. I. Reyero, A. Moral, F. Bimbela, et al., "Metallic Monolithic Catalysts Based on Calcium and Cerium for the Production of Biodiesel," *Fuel* 182 (2016): 668–676, https://doi.org/10.1016/j.fuel.2016.06.043.

58. P. Brussino, J. P. Bortolozzi, O. Sanz, M. Montes, M. A. Ulla, and E. D. Banús, "FeCrAlloy Monoliths Coated With Ni/Al_2O_3 Applied to the Low-Temperature Production of Ethylene," *Catalysts* 8 (2018): 291, https://doi.org/10.3390/catal8070291.

59. R. Abbasi, L. Wu, S. E. Wanke, and R. E. Hayes, "Kinetics of Methane Combustion Over Pt and Pt–Pd Catalysts," *Chemical Engineering Research and Design* 90 (2012): 1930–1942, https://doi.org/10.1016/j.cherd.2012.03.003.

60. H. S. Fogler, "Elements of Chemical Reaction Engineering", in *Prentice Hall International Series in the Physical and Chemical Engineering Sciences*, 3rd ed. (Prentice Hall, 1999).

61. R. J. Madon and M. Boudart, "Experimental Criterion for the Absence of Artifacts in the Measurement of Rates of Heterogeneous Catalytic Reactions," *Industrial & Engineering Chemistry Fundamentals* 21 (1982): 438–447, https://doi.org/10.1021/i100008a022.

62. D. E. Mears, "Diagnostic Criteria for Heat Transport Limitations in Fixed Bed Reactors," *Journal of Catalysis* 20 (1971): 127–131, https://doi.org/10.1016/0021-9517(71)90073-X.

63. J. B. Anderson, "A Criterion for Isothermal Behavior of a Catalyst Pellet," *Chemical Engineering Science* 1 (1963): 147–148.

64. R. S. Kumar, R. E. Hayes, and N. Semagina, "Kinetic Investigation of the Promoting Effect of Cobalt on Pd-Pt/SnO_2 Catalyzed Wet Methane Combustion," *Applied Catalysis A: General* 666 (2023): 119416, https://doi.org/10.1016/j.apcata.2023.119416.

65. X. Fang, B. Liu, K. Cao, et al., "Particle-Size-Dependent Methane Selectivity Evolution in Cobalt-Based Fischer–Tropsch Synthesis," *American Chemical Society Catalysis* 10 (2020): 2799–2816, https://doi.org/10.1021/acscatal.9b05371.

66. W.-J. Wang and Y.-W. Chen, "Influence of Metal Loading on the Reducibility and Hydrogenation Activity of Cobalt/Alumina Catalysts," *Applied Catalysis* 77 (1991): 223–233, https://doi.org/10.1016/0166-9834(91)80067-7.

67. J. Xiong, K. Wu, J. Yang, et al., "The Effect of Existence States of PdOx Supported by Co_3O_4 Nanoplatelets on Catalytic Oxidation of Methane," *Applied Surface Science* 539 (2021): 148211, https://doi.org/10.1016/j.apsusc.2020.148211.

68. J. Xiong, S. Mo, L. Song, et al., "Outstanding Stability and Highly Efficient Methane Oxidation Performance of Palladium-Embedded Ultrathin Mesoporous Co_2MnO_4 Spinel Catalyst," *Applied Catalysis A: General* 598 (2020): 117571, https://doi.org/10.1016/j.apcata.2020.117571.

69. Z. Huang, M. Zhao, J. Luo, et al., "Interaction in LaO_x-Co_3O_4 for Highly Efficient Purification of Toluene: Insight Into LaO_x Content and Synergistic Effect Contribution," *Separation and Purification Technology* 251 (2020): 117369, https://doi.org/10.1016/j.seppur.2020.117369.

70. H. Stotz, L. Maier, A. Boubnov, A. T. Gremminger, J. D. Grunwaldt, and O. Deutschmann, "Surface Reaction Kinetics of Methane Oxidation Over PdO," *Journal of Catalysis* 370 (2019): 152–175, https://doi.org/10.1016/j.jcat.2018.12.007.

71. R. S. Kumar, R. E. Hayes, and N. Semagina, "Effect of Support on Pd-Catalyzed Methane-Lean Combustion in the Presence of Water: Review," *Catalysis Today* 382 (2021): 82–95, https://doi.org/10.1016/j.cattod.2021.07.024.

72. L. S. Escandón, S. Ordóñez, A. Vega, and F. V. Díez, "Oxidation of Methane Over Palladium Catalysts: Effect of the Support," *Chemosphere* 58 (2005): 9–17, https://doi.org/10.1016/j.chemosphere.2004.09.012.

73. R. Kikuchi, S. Maeda, K. Sasaki, S. Wennerström, and K. Eguchi, "Low-Temperature Methane Oxidation Over Oxide-Supported Pd Catalysts: Inhibitory Effect of Water Vapor," *Applied Catalysis A: General* 232 (2002): 23–28, https://doi.org/10.1016/S0926-860X(02)00096-0.

74. P. Marín, S. Ordóñez, and F. V. Díez, "Performance of Silicon-Carbide Foams as Supports for Pd-Based Methane Combustion Catalysts," *Journal of Chemical Technology & Biotechnology* 87 (2012): 360–367, https://doi.org/10.1002/jctb.2726.

Supporting Information

Additional supporting information can be found online in the Supporting Information section.

Supporting File: cctc70646-sup-0001-SuppMat.pdf